RSC Advances

PAPER

View Article Online
View Journal | View Issue

Cite this: *RSC Adv.*, 2025, **15**, 10958

CO_2 methanation over $Ni/SiO_2–Al_2O_3$ catalysts: effect of Ba, La, and Ce addition†

Muhammad Usman, Seetharamulu Podila,* Abdulrahim A. Al-Zahrani and Majed A. Alamoudi

One of the most technologically and financially feasible methods for managing anthropogenic CO_2 emissions is CO_2 hydrogenation to methane. However, the high efficiency of mostly used nickel-based catalysts is still a challenge in the CO_2 methanation process. Herein, 10% silica–90% alumina, commercially known as SIRAL-10, was used as a support for nanostructured Ni catalysts. Modified SIRAL-supported nickel catalysts (Ni/SA) with Ba, La, and Ce metals as promoters were prepared by a simple wet impregnation method. These catalysts were tested for atmospheric CO_2 methanation reaction in a 250–500 °C temperature range in a tubular fixed bed reactor with a H_2/CO_2 molar ratio of 4. As prepared samples were characterized by X-ray diffraction (XRD), Brunauer–Emmett–Teller (BET) analysis, hydrogen temperature-programmed reduction (H_2-TPR), carbon dioxide temperature-programmed desorption (CO_2-TPD), scanning electron microscopy (SEM), energy dispersive X-ray spectroscopy (EDS), and X-ray photoelectron spectroscopy (XPS). CO_2 methanation was found to be highly dependent on surface basic sites and Ni dispersion. Ni active sites were mainly obtained from the reduction of strongly interacted NiO at temperatures >700 °C. All promoted catalysts showed better catalytic activity than unpromoted nickel catalysts. Maximum CO_2 conversion of 85.6% was obtained on the Ba-promoted sample at 400 °C, while low-temperature catalyst activity was achieved in the case of Ce–Ni/SA. The catalysts exhibited CH_4 selectivity in the following order: Ce–Ni/SA > Ba–Ni/SA > La–Ni/SA > Ni/SA. The Ce-containing sample showed exceptional catalytic performance with about 78.4% CO_2 conversion and 98% CH_4 selectivity at 350 °C. Both Ba and Ce-promoted catalysts exposed the best stability for 24 hours. Unique features of the SIRAL support and the addition of basic promoters facilitated the sequential hydrogenation of CO_2 to produce almost CO-free CH_4.

Received 20th December 2024
Accepted 25th March 2025

DOI: 10.1039/d4ra08895f

rsc.li/rsc-advances

1 Introduction

CO_2 methanation is one of the core strategies in "Power to Gas (PtG)" technology that plays a crucial role in achieving carbon neutrality. This pathway uses H_2 and CO_2 to produce methane, which is a major constituent of natural gas.[1,2] The rapid increase in natural gas costs and the depletion of its reserves have increased interest in synthetic or substitute natural gas (SNG) as a clean energy carrier due to its many advantages, including its high combustion efficiency and the ability to utilize existing gas pipelines.[3,4] Modern methanation technology has advanced to the point where it is considerably easier to transform the CO_2 methanation process into industrial-scale.[4,5] However, the extremely exothermic nature of the CO_2 methanation reaction (eqn (1)) makes thermal sintering and stability formidable obstacles, which in turn can reduce the efficiency of the most used catalysts for this process.[6]

$$CO_2 + 4H_2 \leftrightarrows CH_4 + 2H_2O \; \Delta H^0_{298K} = -165.5 \text{ kJ mol}^{-1}; \; \Delta G = -113 \text{ kJ mol}^{-1} \quad (1)$$

Various catalytic systems have been suggested throughout the years to circumvent the kinetic obstacles of the CO_2 hydrogenation to methane.[7–10] Among the catalysts tested, Ru and Ni showed the greatest activity in CO_2 methanation.[11–14] As a result of their inexpensive cost and high CH_4 selectivity, nickel-based catalysts are widely used in hydrogenation of CO_2 to CH_4.[15–19] However, unlike precious Ru-based catalysts, Ni is susceptible to deactivation caused by carbon deposition and nickel sintering.[20]

The type of support greatly affects the distribution of active metallic sites and the interaction between the metal and the support material.[21,22] Recent research has shown that specific acid–base or redox properties of supports can aid in the activation and ensuing transformation of CO_2 and H_2.[23] As a possible support, alumina is utilized because of its large

Chemical and Materials Engineering Department, Faculty of Engineering, King Abdulaziz University, P. O. Box 80204, Jeddah 21589, Saudi Arabia. E-mail: srpodila@kau.edu.sa; Tel: +966 531596482

† Electronic supplementary information (ESI) available. See DOI: https://doi.org/10.1039/d4ra08895f

surface area and excellent thermal stability.[3] Ru/Al_2O_3 is commonly used for low-temperature applications, whereas Ni/Al_2O_3 catalysts, such as those produced by Clariant and BASF, are preferred for situations where temperature control is less crucial.[24] Furthermore, a lot of research on CO_2 methanation with catalysts based on Ni/SiO_2 has been conducted with CO_2 conversion rates ranging from 30 to 90% depending on the catalyst preparation method, Ni loading, and reaction conditions.[25–31] According to the literature,[24,32] incorporating trace amounts of silica into alumina does not alter its chemical surface characteristics, but it does enhance the stability of Al_2O_3 concerning surface area loss and phase transitions of Al_2O_3.[33]. However, at higher loadings, the bulk and surface chemical properties are altered substantially. Zhang *et al.*[34] presented data on a Ni/SiO_2–Al_2O_3 catalyst synthesized using the grinding–mixing process. The catalyst exhibited a 76% conversion of CO with a selectivity of 80% towards CH_4 at 350 °C and a pressure of 2.0 MPa.[34] It was observed that the silica-containing catalyst exhibits higher activity compared to the catalyst supported by bare alumina.

The silica–alumina family of compounds is extremely valuable for adsorption and catalytic applications. Their acid strength can be adjusted by changing Lewis and Brønsted sites. These materials are very stable even at high temperature (>700 °C). They are preferable for some applications due to their decreased inclination to coke.[33] These catalytic supports are highly versatile and beneficial because of their tunable dispersion ability for metal and cationic centers. Due to all these characteristics, silica–alumina materials have been utilized in light olefin oligomerization,[35,36] diesel oxidation catalysts,[37] hydrogenation of conjugated olefins,[38] and CO & CO_2 hydrogenation.[32,39–42] The SIRAL series, made of commercially available amorphous silica–alumina, have been used as possible silica–alumina compounds. By adjusting the silica content, its combined Lewis and Brønsted acidic features can be fine-tuned.[35,43]

According to the literature, the addition of alkaline and alkaline earth metals raised the catalyst basicity to improve CO_2 chemisorption, and the number of oxygen vacancies on the metal surface.[44] Research on Ni/Al_2O_3-based catalysts indicates that Ba is the most effective promoter for CO_2 methanation among Mg, Ca, Ba, and Sr. This is thought to be due to the surface formation of activated *CO and H_2CO* species and a decrease in Ni particle size.[45] The use of lanthanides as promoters to boost catalytic activity has recently exploded in popularity. This is because lanthanides can be highly incorporated into catalyst supports, leading to an increase in nickel dispersion within catalyst frameworks and improved catalytic activity.[45–48] Cerium dioxide exhibits fascinating structural, redox, and alkaline properties and has been extensively employed in diverse applications.[49] It has been shown that catalysts supported by various materials, such as alumina, silica, and zeolites, can enhance their catalytic performance in CO_2 methanation when small quantities of cerium are added.[50–54]

Therefore, in this study, we provide our investigation on the utilization of Ni/SIRAL-10 ($SiO_2 : Al_2O_3$ = 10 : 90 wt%) as a heterogeneous catalyst for the methanation of CO_2. This catalyst can be generated simply and inexpensively by impregnating a Ni precursor on commercially available SIRAL-10. The effect of a small addition of Ba, La, and Ce on SIRAL-supported Ni catalysts is investigated and their physicochemical characteristics are analyzed by using different characterization techniques.

2 Experimental

2.1. Materials

All chemicals were purchased from different suppliers (Table 1) and used without further purification except SIRAL-10, which was calcined at 750 °C for 5 hours in a static air.[24,41]

2.2. Catalyst preparation

All the catalysts were prepared by using the wet impregnation method. The nickel loading was kept constant as 10 wt% for all samples. Nickel precursor was dissolved in an appropriate volume of deionized water and added to the support in a round bottom flask. The impregnation was conducted in a rotary evaporator at 80 °C and 150 rpm for 2 hours. After impregnation the solid dried at 110 °C overnight then calcined the sample at 750 °C for 5 hours with a heating rate of 10 °C min^{-1}.

In a similar fashion, promoted nickel catalysts supported on SIRAL-10 were prepared. Typically, to produce 10 gm of 10% Ni and 4% Ba on SIRAL-10; a solution of 8.6 gm of calcined support and 20 ml of deionized water was taken in a round bottom flask. Before adding nickel salt solution to the support solution, 0.4 gm of barium salt solution was added dropwise so that Ba could mix with acidic support. After that, 4.95 gm of nickel precursor solution was added to it. The final mixture was loaded in a rotary evaporator and then followed the same steps as mentioned above. All catalysts maintained the same loading (4 wt%) of the promoter. Hereafter, SIRAL-10 is denoted as "SA" and promoted-nickel over SIRAL-10 catalysts are designated as "X–Ni/SA (X = Ba, La, Ce)".

Table 1 Chemicals used to prepare catalysts

Reagents	Composition/formula	Purity	Supplier
SIRAL-10	10% SiO_2–90% Al_2O_3	>99%	Sasol (Germany)
Nickel precursor	$Ni(NO_3)_2 \cdot 6H_2O$	99.9%	Fisher chemicals (UK)
Barium precursor	Ba $(NO_3)_2$	99%	Panreac (Spain)
Lanthanum precursor	La $(NO_3)_3 \cdot 6H_2O$	99.9%	Fluka-SIGMA ALDRICH (Austria)
Cerium precursor	$Ce(NO_3)_3 \cdot 6H_2O$	99.9%	Thermo scientific (China)

2.3. Catalyst characterization

The crystal structures of calcined catalysts were investigated using X-ray powder diffraction (XRD) on a Shimadzu X-ray Diffractometer-6100. The diffraction was recorded with Cu-Kα radiation ($\lambda = 1.54056$ Å) in the 2θ range of 20–80°, with a scan speed of 5° min^{-1}. The instrument operated at 30 kV and 30 mA. The crystalline structure size was calculated using Scherrer's equation:

$$D = \frac{k \times \lambda}{\beta \times \cos\theta} \quad (2)$$

where D is crystallite size in nm, k is 0.95 (a constant), λ is wavelength of X-ray (0.1789 nm), β is full width at half maximum (FWHM in radians) and θ is peak position/2 (in radians).

The percentage of metal dispersion of each catalyst was investigated by volumetric CO chemisorption analysis on Autochem 2950 Micromeritics apparatus. The detailed procedure is described in ESI and ref. 55.† The following equation[56] was used to determine Ni dispersion (%).

$$D = \frac{SF \times n \times MW \times 10^2}{W \times wt\%} \quad (3)$$

where, SF = CO/Ni = 1; n mole of active gas adsorbed; MW is molecular weight of the particle (g mol^{-1}); W = total weight of sample; wt% = weight % of metal in sample (*i.e.* 10%).

The surface area and pore size distribution of calcined catalysts were determined using the NOVA 2200e (manufactured by Quantachrome Instruments). The measurements were conducted at −196 °C. Prior to measurement, the samples underwent degassing at 200 °C for 2 hours under vacuum.

The H_2-TPR experiments were conducted using a Micromeritics Autochem II 2950 apparatus with a thermal conductivity detector (TCD) at atmospheric pressure. Firstly, 0.1 g of calcined catalyst was loaded in a U-shaped quartz tube. Subsequently, the catalyst temperature raised linearly from room temperature to 120 °C under helium (He) with a flow rate of 15 ml min^{-1} and kept on the same condition for 60 minutes. This pretreatment step aimed to eliminate physically adsorbed water on the catalyst. Next, the catalyst was cooled down to 40 °C in the He environment. Finally, the analysis was conducted by heating the sample to 850 °C at a rate of 10 °C min^{-1}. This analysis was carried out in a gas mixture of 10% hydrogen and 90% argon, with a flow rate of 40 ml min^{-1}.

Temperature-programmed desorption with carbon dioxide (CO_2-TPD) analyses were performed to assess the basicity of synthesized catalysts. The experiments conducted on the same instrument were used for H_2-TPR analysis. Before analysis, 0.1 g of catalyst was reduced with 10% H_2 and 90% Ar gas mixture (50 ml min^{-1}) and subsequently, the catalyst was flushed with He gas. Next, the sample temperature was cooled to 40 °C under He flow. After that, the 10% CO_2/He mixture gas was used to adsorb on the surface of reduced samples for 1 h at 40 °C. After completion of adsorption, the sample was flushed with He gas for one hour to remove physisorbed CO_2. Then the temperature of the sample raised progressively at a ramping rate of 10 °C per minute from 40 °C to 850 °C.

The catalysts' surface morphology was examined using a scanning electron microscope (JSM-IT500 integrated with EDX). Using energy dispersive X-ray spectroscopy, an elemental composition analysis was performed to estimate the weight percentages of Ni, Ba, La, and Ce on SiO_2–Al_2O_3.

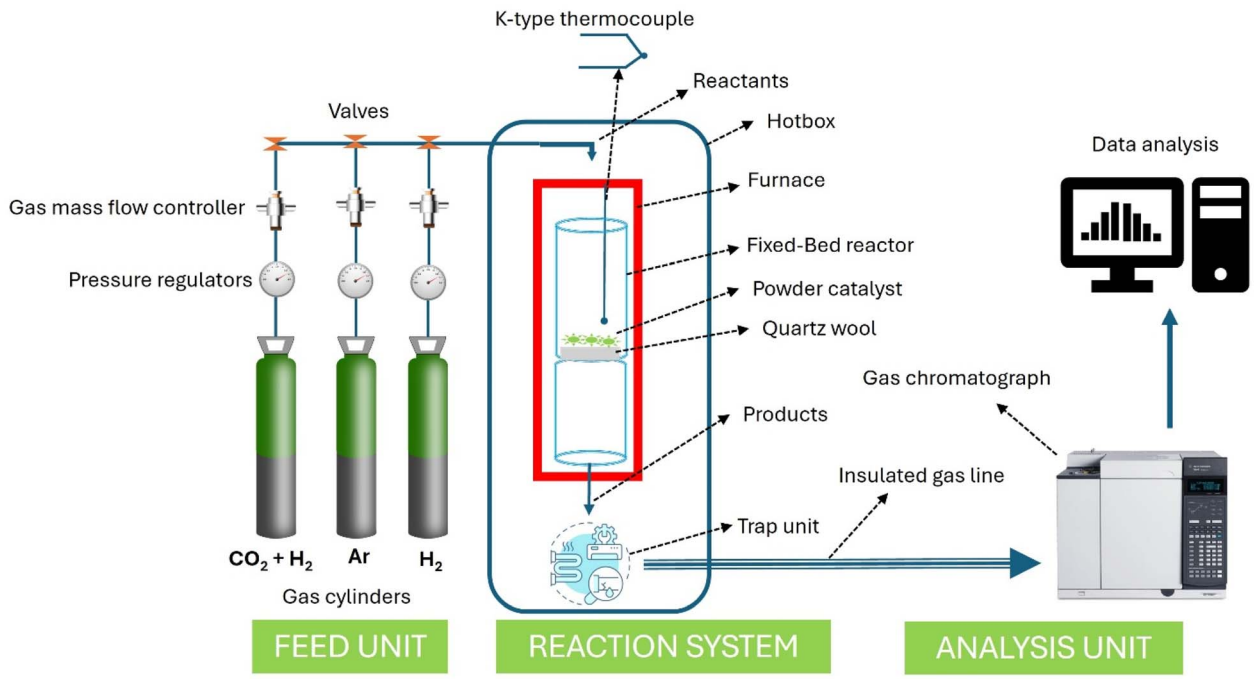

Fig. 1 Experimental setup for the CO_2 methanation reaction.

X-ray photoelectron spectroscopy (XPS) was used to investigate the surface elemental composition of the calcined catalysts. Finely crushed samples were evaluated using Mg-Kα X-ray source in Specs GmbH (Berlin, Germany) equipment. The C 1s peak at around 285.0 eV was used for charge referencing to mitigate charging effects. XPSPEAK41 software was used to deconvolute the spectra peaks. Following the elimination of the non-linear (Shirley) background, high-resolution core-level spectra was utilized for quantitative surface chemical studies.

2.4. Catalyst activity

The CO_2 methanation reaction was carried out at atmospheric pressure using MA-Effi (PID Eng & Tech, Spain) vertical continuous-flow fixed-bed reactor with an inner diameter of 9.1 mm and a length of 300 mm. Mass flow controllers (Bronkhorst) were used to regulate the movement of the feed gases. A k-type thermocouple was utilized to monitor the precise reaction temperature of the catalyst, which was positioned at the center of the tubular reactor, as shown in Fig. 1. A quantity of 300 mg of catalyst was placed onto quartz wool. The reactor's temperature was brought up to 750 °C at a rate of 10 °C min^{-1} under an Ar flow of 20 ml min^{-1}. The catalyst was subjected to an *in situ* reduction process at 750 °C and 1 atm followed by a half-hour exposure to a flow of 20 ml min^{-1} of 99.99% pure hydrogen gas, prior to the reaction. The reduction conditions were adopted by referring to previous works of Riani *et al.*[24,41] about Ni/SiO_2–Al_2O_3 for CO_2 methanation. After reduction, the temperature was reduced to 250 °C (initial reaction temperature) and the mixture of H_2 and CO_2 (with a molar ratio of $H_2/CO_2 = 4/1$) was fed into the reactor at a gas hourly space velocity (GHSV) of 12 000 ml g^{-1} h^{-1}. The catalytic experiments were conducted at various temperatures spanning from 250 to 500 °C with an increment of each 50 °C. Products were analyzed after 0.5 hours at each temperature, and an average of three readings is reported.

An online gas chromatogram (Agilent 7890 B) equipped with a thermal conductivity detector (TCD) and a flame ionization detector (FID) was used to evaluate gas products. CO_2, CO, and CH_4 were analyzed by using TCD with a HayeSep Q-packed column. An FID detector with an HP-Pona capillary column (19091S-001E) was also employed for CH_4 detection. Following equations[57,58] were used to determine the CO_2 conversion (X_{CO_2}), CH_4 selectivity (S_{CH_4}), CO selectivity (S_{CO}), and yield (Y) of methane.

$$X_{CO_2}(\%) = \frac{CO_2(in) - CO_2(out)}{CO_2(in)} \times 100 \quad (4)$$

$$S_{CH_4}(\%) = \frac{CH_4(out)}{CH_4(out) + CO(out)} \times 100 \quad (5)$$

$$S_{CO}(\%) = \frac{CO(out)}{CH_4(out) + CO(out)} \times 100 \quad (6)$$

$$Y(\%) = \frac{X_{CO_2} \times S_{CH_4}}{100} \quad (7)$$

where (in) and (out) represent the molar flow rate of respective gas at the inlet and outlet of the reactor. The data reported for conversion and selectivity were obtained by an average of three readings at one temperature. In order to calculate the consumption rate of CO_2 (mol_{CO_2} g_{cat}^{-1} s^{-1}) at lower reaction temperatures, the following equation[59] was used:

$$r_{CO_2}(\%) = \frac{X_{CO_2}}{100} \times \frac{F_{CO_2}}{W_{cat}} \quad (8)$$

where F_{CO_2} and W_{cat} represent the molar flow rate of CO_2 at the inlet (mol s^{-1}) and weight of catalyst (g) respectively. Long-term stability was analyzed on the best-performing X–Ni/SA catalyst at an optimum temperature.

3 Results and discussion

3.1. Physiochemical characteristics of calcined catalysts

The powder XRD patterns of all calcined samples and support SA (10% SiO_2–90% Al_2O_3) are shown in Fig. 2. Support sample revealed two clear diffraction peaks at $2\theta = 66.7°$, 46.5° and 37.64° representing γ-Al_2O_3.[35] These peaks correspond to the alumina crystal plane of (440), (400) and (311) respectively (PDF#10-0425).[60] All Ni/SA samples showed peaks at $2\theta = 37.5°$ corresponding to the (111) plane of the NiO phase, consistent with previous studies.[28,61,62] The appearance of sharp peak at 37.5° for all samples excluding the support shows that the presence of NiO formed by calcination at higher temperature (750 °C). The γ-Al_2O_3 peaks remained the same at both positions, but a small shift towards the lower angle and peak broadening observed in Ba, La and Ce promoted Ni/SA samples.

In the case of Ce promoted sample, CeO_2 (111) plane at 28.5° and CeO_2 (311) peak at $2\theta = 56.3°$ were observed (PDF#034-0394).[63–65] A minor shift toward lower angle from $2\theta = 46.5°$ to

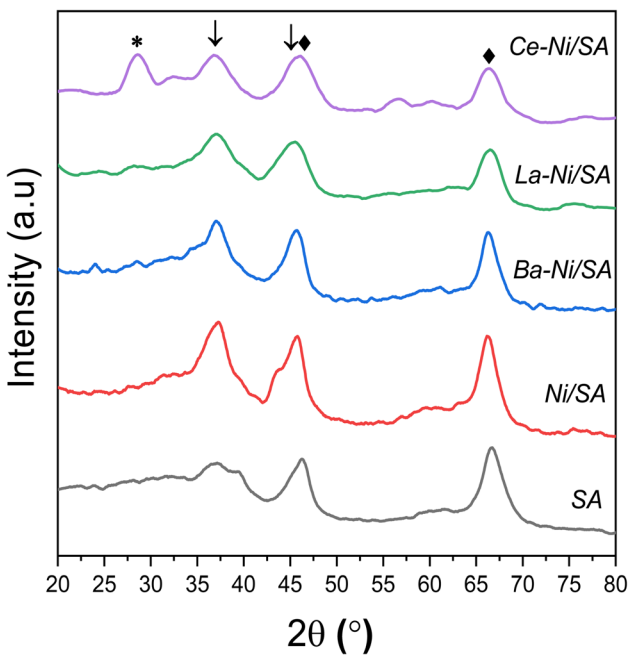

Fig. 2 XRD patterns of calcined catalysts ◆-γ-Al_2O_3 [PDF#10-0425], *-CeO_2 [PDF#034-0394], ↓-NiO [PDF#044-1159].

45° and from 67.4° to 66° in the case of Ce promoted sample is correlated with the gradual incorporation of Ni^{2+} into the Al–O crystal structure.[66] No XRD signal at 28.2° observed corresponds to La_2O_3 (JCPDS 065-3185) or $La(OH)_3$ (JCPDS 13-1481).[67,68] This might be due to low crystal size or amorphous in nature. In the case of all promoted catalysis, broadening of diffraction peak of NiO at 37.5° was observed which might be due to the transformation of NiO to $NiAl_2O_4$ as described in previously reported Ni over silica doped alumina catalysts.[32,41]

The crystallite size and FWHM values of NiO are listed in Tables 2 and S2,† respectively. Lower Ni crystal size in promoted samples showed that addition of small amount of Ba, La and Ce is beneficial in increasing Ni dispersion on the silica–alumina support.

These results are in good correlation with CO chemisorption data displayed in Table S3† where we observed that the order of Ni average particle size in the catalyst samples is Ba–Ni/SA > Ni/SA > La–Ni/SA > Ce–Ni/SA.

Low temperature nitrogen adsorption and desorption experiments were performed to analyze textural properties of synthesized catalysts. A summary of obtained results is presented in Table 2. The addition of Ni on support (SA) results in decreased BET surface area and pore volume from 339 to 276 $m^2 g^{-1}$ and 0.71 to 0.61 $cm^3 g^{-1}$ respectively. This is due to blocking of support pores with Ni during preparation of Ni/SA catalyst.[35] The introduction of promoters in Ni/SA the surface area and total pore volume further lowered. This is because the promoter loading causes a partial blockage of the support's pores. Maximum decline was experienced in the case of Ba promoted sample. It is interesting to observe that the pore size of Ce containing sample was more than all other samples including support. The interaction between Ni and CeO_2 may be the reason for the larger pore size in the Ce-containing sample. This interaction alters the structure of support, facilitating the creation of oxygen vacancies.[66] CeO_2 has the capacity to produce oxygen vacancies and is well-known for its strong oxygen mobility; these properties can impact how Ni particles sinter during catalyst synthesis.[69] These interactions may cause the support structure to reorganize, which in turn may alter the pore size and distribution. Increased mesopore size could be due to improved thermal stability and resistance to pore collapse on the Ce containing Ni/SA. The XRD study further indicated that the crystalline size of NiO in Ce–Ni/SA is smaller than that of other samples, which could lead to a bigger pore size.[51] All samples exhibited type IV (a) isotherm and H1 hysteresis loop according to IUPAC isotherm classification (Fig. 3a) indicating mesoporous solids with open and some partially blocked pores.[70]

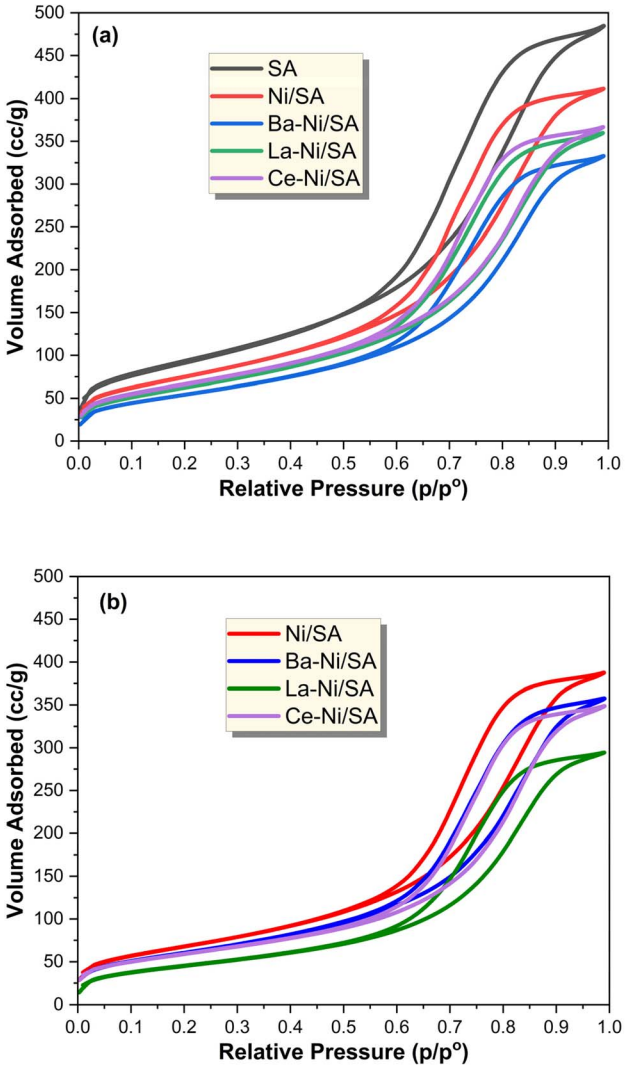

Fig. 3 Nitrogen adsorption–desorption isotherms of (a) fresh calcined catalysts (b) spent catalysts after reaction.

Table 2 Texture properties of calcined SA support, Ni/SA, and X–Ni/SA catalysts

Catalyst	Surface area[a] ($m^2 g^{-1}$)	Pore volume[b] ($cm^3 g^{-1}$)	Pore size[b] (nm)	Total H_2 consumption[c] ($\mu mol\ g^{-1}$)	Total CO_2 desorption[d] ($\mu mol\ g^{-1}$)	NiO crystalline[e] size (nm)	Metal dispersion[f] (%)
SA	339	0.71	5.7	—	471.24	—	—
Ni/SA	276	0.61	5.7	761.27	975.61	3.84	5.33
Ba–Ni/SA	203	0.49	5.68	765.95	624.69	4.46	4.16
La–Ni/SA	234	0.53	5.68	817.85	585.39	3.30	5.62
Ce–Ni/SA	245	0.54	6.24	692.48	912.99	2.99	5.98

[a] Calculated by BET method from N_2 adsorption–desorption analysis. [b] Calculated by BJH method from N_2 adsorption–desorption analysis. [c] Obtained from H_2-TPR results from 100–850 °C range. [d] Obtained from CO_2-TPD results from 100–850 °C range. [e] Calculated from XRD profiles of calcined sample at $2\theta = 37.5°$. [f] Estimated by CO pulse chemisorption analysis.

Relative saturation point (p/p_o) detained at about 0.85 for all samples and for promoted catalysts a slight shift to 0.8 was observed. The occurrence of a hysteresis loop at high relative pressure ($p/p_o > 0.7$) indicates mesopores.[71] There is no change observed in isotherm patterns in promoted catalysts comparison to that of Ni/SA catalyst. The pore size distribution of all samples is shown in Fig. 3b, representing a narrow distribution with pore diameter below 10 nm. Fig. 3B shows the outcomes of the physisorption isotherms for the spent catalysts. While the surface area values changed, the N_2 adsorption–desorption isotherm patterns remained unchanged in the exhausted catalysts. The surface area values of all the spent catalysts decreased, except for Ba–Ni/SA, whose surface area rose from 203 to 220. The reduction of surface area might be due to the agglomeration of Ni particles on the surface[72] and blockages of some mesopores.[42] An increase in surface area after the reaction in the case of Ba containing sample might be due to the structural changes with enlargements of pores.[73]

Table S1† lists the BET surface area, pore volume, and pore size values of all the used catalysts.

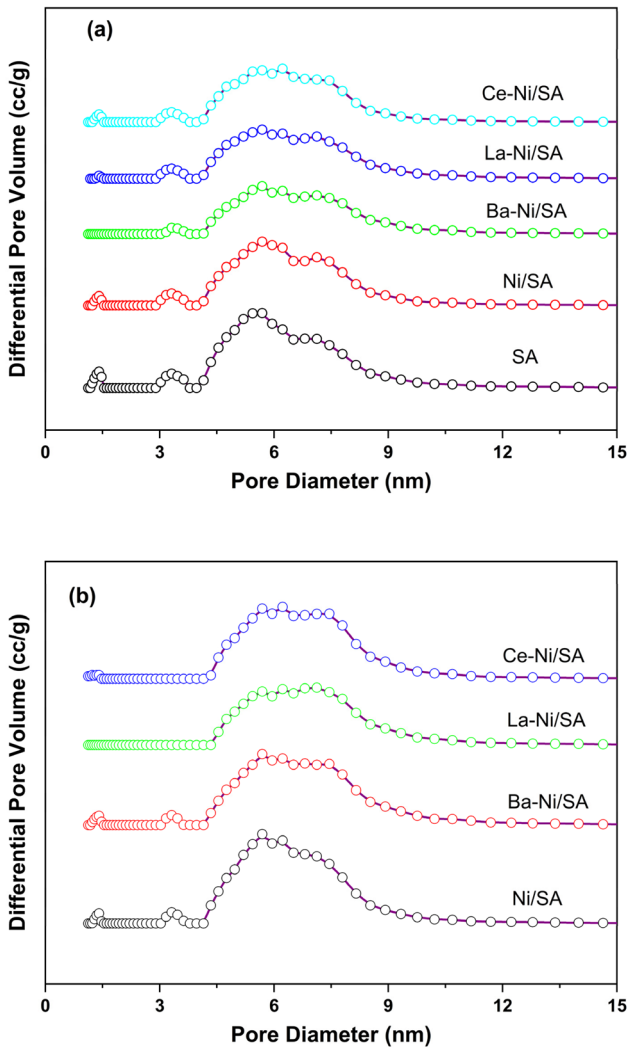

Fig. 4 Pore size distribution for the catalysts (a) before reaction (b) after reaction.

Hydrogen temperature-programmed reduction (H_2-TPR) was conducted to evaluate the reducibility and metal–support interactions of the synthesized catalysts. The H_2-TPR profiles for both unpromoted and promoted nickel catalysts are presented in Fig. 4a. All catalysts exhibited a single reduction peak above 700 °C, indicating the presence of strongly interacting Ni^{2+} species with the support. Based on literature, high-temperature reduction peaks for Ni^{2+} can be attributed to two distinct species: (1) Ni^{2+} ions with strong direct interactions with the support and/or promoter, and (2) Ni^{2+} ions within the $NiAl_2O_4$ spinel phase.[74] On other hand, some studies have reported low-temperature reduction peaks in nickel-based catalysts, corresponding to weakly interacting or bulk NiO, alongside the high-temperature peaks. This observation is typically associated with higher nickel loadings, which can lead to the formation of less dispersed NiO phases.[42]

Table 2 presents hydrogen consumption for all catalysts. Notably, the total hydrogen consumption decreased upon the introduction of promoters. This reduction likely stems from increased NiO dispersion and enhanced interaction between NiO and the promoters & support. Among the promoted catalysts, La–Ni/SA exhibited the highest hydrogen consumption, potentially due to lanthanum facilitating the reduction of a greater proportion of Ni^{2+} species compared to barium and cerium promoted catalysts.[75,76]

Temperature Programmed Desorption (TPD) experiments were performed to analyze the total basicity of all prepared samples including the support. CO_2 is a weak Lewis acidic molecule that can be absorbed on certain basic catalyst sites during the hydrogenation process. Adsorption of CO_2 is used to recognize the strength and type of basic sites present in the catalyst. Reaction temperature is another factor that determines the adsorbed quantity.[77,78] In the case of monometallic (unpromoted) sample, the Lewis basic sites of Ni and the Brønsted basic hydroxyl groups of the Al_2O_3 can adsorb CO_2.[79] The addition of promoter could form additional metal bicarbonates and shift the nature of catalysts[80] Using TPD analysis up to 850 °C, we determined the amount of CO_2 adsorbed at temperatures that are kinetically relevant for methanation. CO_2-TPD profiles of all reduced samples are presented in Fig. 4b, while quantitative results are shown in Table 2. There are two clear peaks in the CO_2 desorption profile: one at low temperatures (around 90–110 °C) and another at high temperatures (about 350 °C). The first peak represents physiosorbed CO_2 (weak basicity) on SA surface. While the second peak suggested the chemisorption of CO_2 on medium and strong basic sites.[81] No more desorption peaks were observed for all samples until reaching 850 °C.

The amount of CO_2 desorption was low on SA support, indicating mildly acidic nature of silica–alumina support. Impregnation of Ni on SA enhances the amount of CO_2 desorption and peak maxima was shifted from around 360 °C to about 280 °C, showing the moderated basic nature of Ni supported catalyst. For all promoted samples, CO_2 desorption value was increased, and maximum desorption peak was shifted toward lower temperature. The order of total basicity was found to be as: Ni/SA > Ce–Ni/SA > Ba–Ni/SA > La–Ni/SA > SA.

According to the literature, the presence of strong basic sites does not favor methanation process, probably because CO_2 sticks to the basic sites too tightly at reaction temperature, allowing it to be captured instead of converted.[71,81,82]

The surface morphology of the as prepared X–Ni/SA samples and pure SA support are presented in Fig. S4 and S5† respectively. Surface morphology of unpromoted Ni/SA is changed from irregular spherical form to spherical clusters with aggregates after the addition of La and Ba promoters. Plates like structures appeared at La and Ba containing samples. These agglomerations might be due to the basic nature of La and Ba, further discussed in XPS analysis. Ce–Ni/SA exhibits roughly spherical structure suggesting absence of any agglomeration of the particles on silica–alumina support.

The expected elemental composition in SA supported catalysts is indicated by the EDS peaks. With a uniform distribution of essential elements and effective dispersion, EDS analysis validates the theoretical weight% of Ni and promoters used during the synthesis of X–Ni/SA catalysts. In all samples, wt% of Ni was found above 8% while wt% of promoter was found above 3%, as shown in Fig. S4.† Overall, the SEM and EDS findings suggest that applied synthesis method for preparation of SiO_2–Al_2O_3 supported Ni catalysts was appropriate.

X-ray photoelectron spectroscopy is a powerful surface analysis technique that provides information about the outermost few nanometers of heterogenous catalysts responsible for reaction. Species and their oxidation states present on the surface of X–Ni/SA catalysts were identified using XPS. Fig. 6 displays the Ni 2p spectra, which provides insights into the surface state of the active nickel species. The high-resolution XPS spectra of Ni $2p_{3/2}$ revealed three distinct peaks at binding energies of 853 eV, 856.5 eV, and 861 eV. Riani *et al.*[41] investigated the interaction of Ni with SiO_2–Al_2O_3 and reported that the presence of SiO_2 in the support inhibits the formation of $NiAl_2O_4$, leading to the existence of two distinct Ni^{2+} species in the catalysts. Similarly, De Piano *et al.* examined the interaction of Ni with Al_2O_3 in the presence of Ce as a promoter. Their findings indicate the presence of two types of Ni^{2+} species: one exhibiting strong interaction with the support and the other forming Ni–O_x–Ce interfacial interactions.[66,83] Numerous other studies have also reported the existence of various Ni^{2+} species in Ni/Al_2O_3 catalysts with different promoters.[84–88] Based on these literature reports, the peaks observed in Fig. 6 can be attributed to different Ni^{2+} species, including direct interaction with the support, interface interactions with promoters (such as Ni–Ce and Ni–La), and Ni^{2+} species associated with $NiAl_2O_4$. In a barium-containing sample, the Ni 2p XPS signal observed at 860.9 eV could indicate the presence of NiO or a barium-interacted nickel species.[89] This interaction may alter the sample's electronic environment, influencing the nickel binding energy. Notably, the binding energies of Ni^{2+} species are higher in Ba–Ni/SA catalysts compared to Ce–Ni/SA catalysts, suggesting a change in the nickel interaction strength due to the promoter, shifting from barium to cerium.

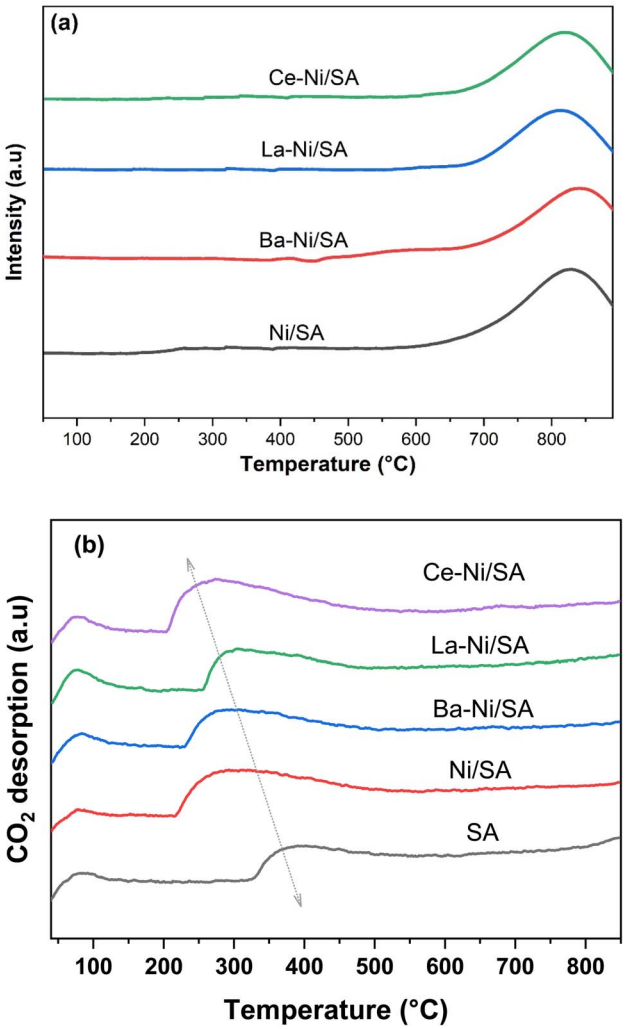

Fig. 5 (a) H_2-TPR and (b) CO_2-TPD profiles of X–Ni/SA catalysts.

High-resolution XPS spectra of O 1s (Fig. 7) for all X–Ni/SA samples revealed two distinct peaks, corresponding to lattice oxygen (530 eV) and absorbed oxygen species (535 eV). Notably, the O 1s spectra of Ni/SA and Ba–Ni/SA exhibited no significant differences. Similar results were reported by Ayub *et al.*[58] In contrast, La–Ni/SA and Ce–Ni/SA samples showed a significant

Table 3 Atomic percentage of each element on surface of catalysts, obtained by XPS

Catalyst	Ni $2p_{3/2}$	O 1s	Al $2p_{3/2}$	Si $2p_{3/2}$	C 1s	Ce $4d_{5/2}$	Ba $3d_{5/2}$	La $4d_{5/2}$
Ni/SA	19.08	23.22	22.28	12.39	23.03	—	—	—
Ce–Ni/SA	18.29	25.22	20.62	11.35	18.31	6.21	—	—
Ba–Ni/SA	16.88	18.98	20.80	15.68	20.39	—	7.27	—
La–Ni/SA	13.39	20.32	23.72	11.71	28.65	—	—	2.21

increase in the intensity of the adsorbed oxygen peak. This adsorbed oxygen signal (OH^-) is attributed to oxygen species trapped by electron-rich oxygen vacancies, with its intensity directly correlating to the surface oxygen vacancy concentration.[90] The enhanced adsorbed oxygen peak in Ce–Ni/SA indicates stronger electronic interactions within this catalyst. To further understand the impact of the promoter on Ni/SA, surface atom quantification was performed, and the results are summarized in Table 3. The atomic-oxygen content followed the trend: Ce–Ni/SA > Ni/SA > La–Ni/SA > Ba–Ni/SA. This suggests that Ce–Ni/SA possesses a higher concentration of surface oxygen vacancies, facilitating the adsorption of gaseous oxygen.[65]

Surface active metal (Ni) percentages were high in Ce and Ba promoted, at 18% and 16%, respectively. Al 2p3/2 XPS spectra of all calcined samples are shown in Fig. S1.† As expected from the quantification results, the highest Al peak was observed at 78 eV in the case of Ni–La/SA.

3.2. Catalytic performance in CO_2 methanation

The CO_2 conversion and CH_4 selectivity for each catalyst are presented in Fig. 8. The main products detected were CH_4 and CO, confirming the occurrence of both CO_2 methanation (eqn (1)) and the reverse water-gas shift (RWGS) reaction (eqn (9)). The CO_2 conversion and CH_4 selectivity increased with temperature, reaching their highest values at 400 °C, beyond which selectivity declined due to increased CO production *via* RWGS. This trend aligns with previous findings on Ni-based catalysts, where higher temperatures favor CO formation over CH_4 due to thermodynamic limitations.[27]

$$CO_2 + H_2 \leftrightarrows CO + H_2O\ \Delta H^0_{298K} = +41\ \text{kJ mol}^{-1} \quad (9)$$

The monometallic Ni/SA catalyst exhibited moderate CO_2 conversion, reaching 61.2% at 400 °C, but suffered from lower CH_4 selectivity (84.7%) due to significant CO formation. Maximum CO selectivity was observed in monometallic Ni/SA

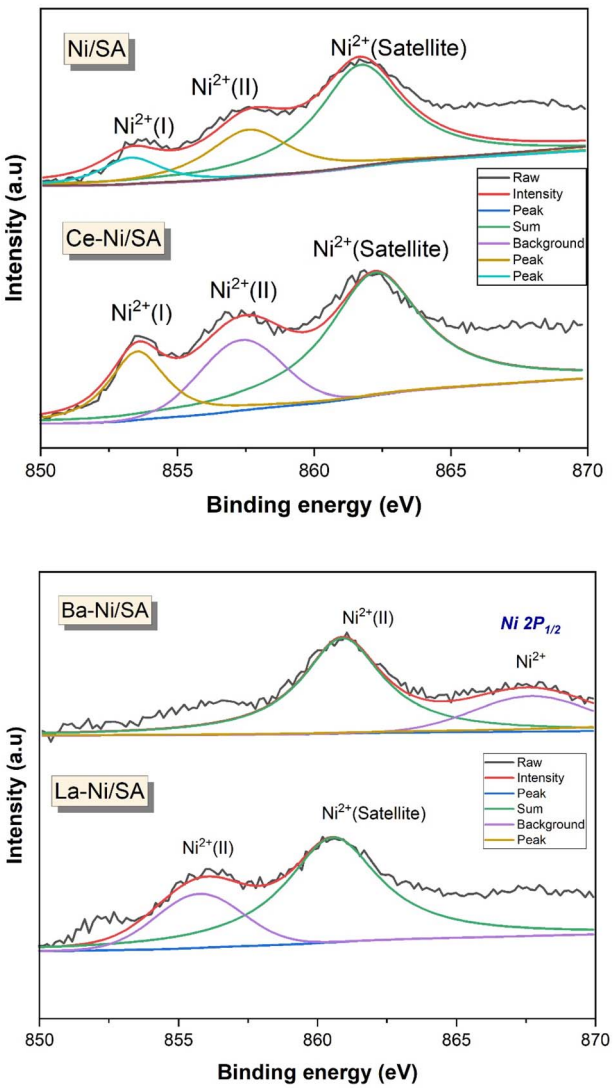

Fig. 6 Ni 2p XPS spectra of calcined X–Ni/SA catalysts.

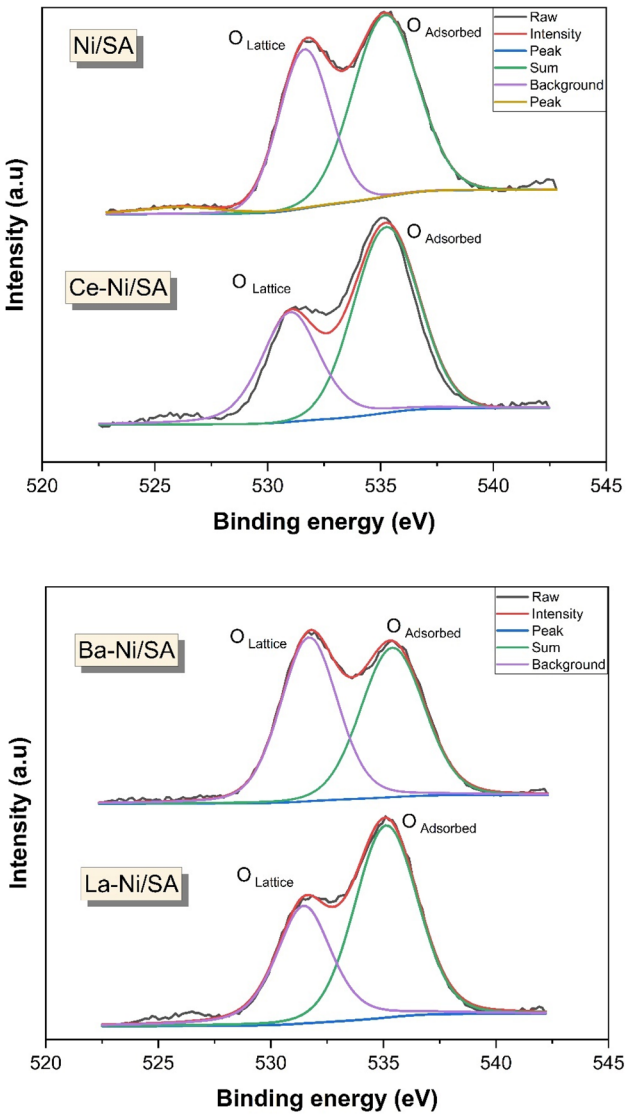

Fig. 7 O 1s XPS spectra of calcined X–Ni/SA catalysts.

sample (Fig. S3†). After introducing promoters (Ba, La, and Ce), both CO_2 conversion and CH_4 selectivity improved significantly. The Ce–Ni/SA catalyst exhibited the highest CH_4 selectivity (97.5% at 350 °C), while Ba–Ni/SA achieved the highest CO_2 conversion (85.6% at 400 °C). The product yield was higher on Ce–Ni/SA at lower temperatures till 350 °C (Fig. S2†). The superior low-temperature activity of Ce–Ni/SA can be attributed to smaller NiO crystallite size (2.99 nm) (Table 2), leading to higher Ni dispersion and more active sites,[91] formation of oxygen vacancies, and moderate basicity,[84] ensuring effective CO_2 adsorption while avoiding excessive carbonate formation that could hinder reaction kinetics (from CO_2-TPD results). These findings match with studies reporting that Ce-doped Ni catalysts exhibit enhanced methanation activity at lower temperatures (<400 °C) due to oxygen vacancies and better Ni dispersion.[6,51,66,91] In contrast, Ba–Ni/SA showed the highest CO_2 conversion at 400 °C due to enhanced CO_2 adsorption capacity (Fig. 5b), which facilitated surface hydrogenation. This behavior aligns with previous reports where alkaline earth metal promoters increase CO_2 chemisorption, boosting conversion at higher temperatures.[44,86] The La–Ni/SA catalyst, while improving over the unpromoted Ni/SA, showed relatively lower CO_2 conversion (78.9% at 400 °C) and CH_4 selectivity (93.4%). This could be due to its strong Ni–support interactions, leading to larger NiO crystallites (3.3 nm) and lower reducibility, as indicated by H_2-TPR analysis (Fig. 5a). In summary, the best catalytic activity of Ce–Ni/SA sample can be attributed due to interaction of Ce with Ni^{2+} on SA support (from XPS results), large amount of medium basic sites and more oxygen vacancies that provide sites for hydrogen dissociation result in considerably higher CH_4 selectivity.[66]

To evaluate the catalyst performance under long-term operation, Ce–Ni/SA and Ba–Ni/SA were tested for 24 hours at 400 °C (Fig. 10). Both catalysts exhibited stable CH_4 selectivity, with Ba–Ni/SA maintaining 85.6% CO_2 conversion, while Ce–Ni/SA showed a slight decline (2.5%) due to minor deactivation,

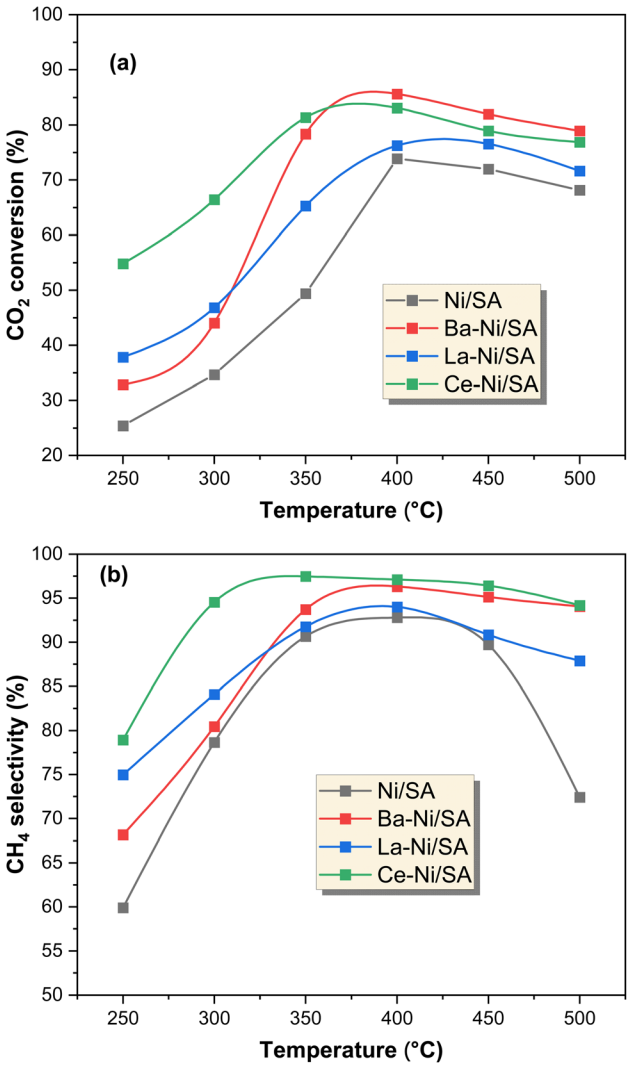

Fig. 8 Catalytic activity results of X–Ni/SA catalysts at 1 atm, 250–500 °C, 12 000 ml g^{-1} h^{-1}, $H_2/CO_2 = 4/1$; (a) CO_2 conversion, (b) CH_4 selectivity.

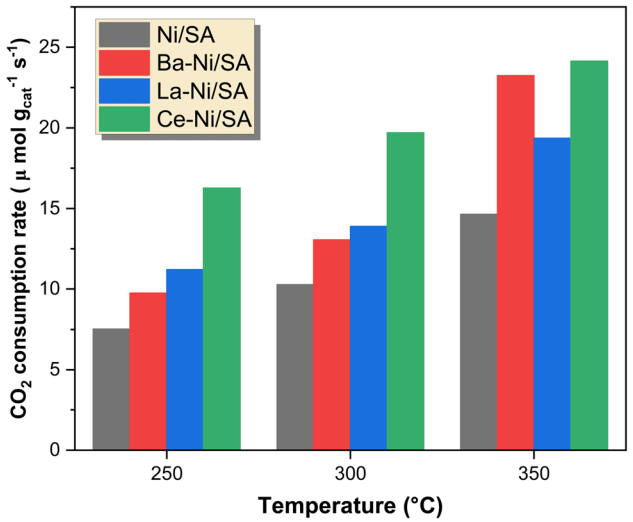

Fig. 9 CO_2 consumption rates at three initial temperatures.

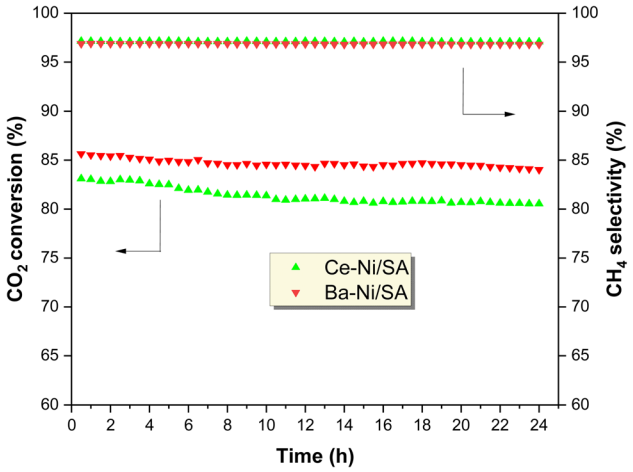

Fig. 10 Catalyst stability of Ce and Ba promoted Ni/SA catalysts at 400 °C.

Table 4 Catalyst performance comparison with previously published literature

Catalyst	Reaction conditions	Performance	Ref.
13.6% Ni/20% SiO_2–80% Al_2O_3	T = 250–500 °C; P = 1 atm GHSV = 55 000 h^{-1}; H_2/CO_2 = 5	X_{CO_2} = ~66% S_{CH_4} = ~100%; at 400 °C	24
10% Ni/SiO_2	T = 200–450 °C; P = 1 atm GHSV = 2400 h^{-1}; H_2/CO_2 = 4	X_{CO_2} = 68% S_{CH_4} = 66%; at 400 °C	92
Ni-0.25% Mn/SIRAL-20 (20% SiO_2–Al_2O_3)	T = 200–400 °C; P = 20 bar GHSV = 60 000 ml g^{-1} h^{-1}; H_2/CO_2 = 4	X_{CO_2} = 83% S_{CH_4} = >95% at 300 °C	39
30% Ni/0.25% SiO_2–99.75% Al_2O_3	T = 200–500 °C; P = 1 atm GHSV = 9000 ml g^{-1} h^{-1}; H_2/CO_2 = 3.5	X_{CO_2} = 82% S_{CH_4} = 96% at 350 °C	93
10% Ni/SiO_2	T = 200–400 °C; P = 1 atm GHSV = 30 L g^{-1} h^{-1}; H_2/CO_2 = 4	X_{CO_2} = 67% S_{CH_4} = 94% at 350 °C	94
40% Ni/SiO_2	T = 290–470 °C; P = 1 atm GHSV = 10 000 ml g^{-1} h^{-1}; H_2/CO_2 = 4	X_{CO_2} = 30% S_{CH_4} = 83% at 330 °C	42
13.6% Ni/1% SiO_2–99% Al_2O_3	T = 250–500 °C; P = 1 atm GHSV = 55 000 h^{-1}; H_2/CO_2 = 5	X_{CO_2} = ~79% S_{CH_4} = ~100%; at 400 °C	24
5% Ni–5% Ba/Sm_2O_3	T = 200–450 °C; P = 1 atm GHSV = 2400 ml g^{-1} h^{-1}; H_2/CO_2 = 4	X_{CO_2} = 72.7% S_{CH_4} = 100% at 450 °C	58
10% Ni/(Al_2O_3–ZrO_2)	T = 160–460 °C; P = 1 atm GHSV = 6000 ml g^{-1} h^{-1}; H_2/CO_2 = 4	X_{CO_2} = 77% S_{CH_4} = 100% at 340 °C	95
15% Ni–1% Ru/Al_2O_3	T = 250–550 °C; P = 1 atm GHSV = 5835 h^{-1}; H_2/CO_2 = 5	X_{CO_2} = 88% S_{CH_4} = 93% at 400 °C	96
10% Ni–5% Ce/Al_2O_3	T = 50–650 °C; P = 1 atm GHSV = 7200 h^{-1}; H_2/CO_2 = 4	X_{CO_2} = 72% S_{CH_4} = 98% at 400 °C	97
10% NiO/(CaO–Al_2O_3)	T = 250–550 °C; P = 1 atm GHSV = 18 000 ml g^{-1} h^{-1}; H_2/CO_2 = 4	X_{CO_2} = 79.1% S_{CH_4} = 98.1% at 450 °C	98
10% Ni–4% Ce/SIRAL-10	T = 250–500 °C; P = 1 atm GHSV = 12 000 ml g^{-1} h^{-1}; H_2/CO_2 = 4	X_{CO_2} = 81.3% S_{CH_4} = 97.5% at 350 °C	This work
10% Ni–4% Ba/SIRAL-10	T = 250–500 °C; P = 1 atm GHSV = 12 000 ml g^{-1} h^{-1}; H_2/CO_2 = 4	X_{CO_2} = 85.6% S_{CH_4} = 96% at 400 °C	This work

possibly a lower Ni–Ce interactions at high temperatures. Furthermore, CO_2 consumption rates at 250–350 °C (Fig. 9) confirmed that Ce–Ni/SA exhibited the highest reaction rate at lower temperatures, correlating well with its high Ni dispersion and oxygen vacancies. Table 4 compares the performance of our catalysts with previously reported Ni-based systems. The Ce–Ni/SA catalyst (97.5% CH_4 selectivity at 350 °C) and Ba–Ni/SA (85.6% CO_2 conversion at 400 °C) outperform many reported catalysts in terms of low-temperature CH_4 selectivity and overall CO_2 conversion, confirming the effectiveness of SIRAL-10 support and strategic promoter selection.

4 Conclusions

The catalytic activity was increased with a small addition of Ba, La and Ce on SiO_2–Al_2O_3 supported Ni catalysts for CO_2 methanation. The 10% Ni–4% Ce/SIRAL-10 catalyst displayed the highest CO_2 methanation activity at 250–400 °C. Upon the addition of promoter, the incorporation of Ni into Al_2O_3 and oxygen vacancies increased. At high temperatures the Ba promoted catalyst is more active than the Ce promoted catalyst. The addition of Ce to the catalyst system plays a crucial role in optimizing Ni dispersion and preventing sintering. This dual function leads to catalysts with high activity and durability. The best catalytic activity of Ce–Ni/SA sample can be attributed due to better reducibility, high N^{2+} incorporation on SA support, large amount of medium basic sites and more oxygen vacancies that provide sites for hydrogen dissociation result in considerably higher CH_4 selectivity. This study presents a simple preparation method to use silica–alumina class of compounds as a prospective support material for Ni-based catalysts for efficient CO_2 conversion to methane.

Data availability

All the data concerning this study added in the manuscript. There is no additional data available for the manuscript.

Conflicts of interest

There are no conflicts to declare.

Acknowledgements

This project was funded by KAU Endowment (WAQF) at King Abdulaziz University, Jeddah, under grant no. WAQF:217-135-2024. The authors, therefore, acknowledge with thanks WAQF and the Deanship of Scientific Research (DSR) for technical and financial support.

References

1 R. Zhu, Q. Liu, Y. He and P. Liang, *J. Colloid Interface Sci.*, 2024, **668**, 352–365.
2 U. Ulmer, T. Dingle, P. N. Duchesne, R. H. Morris, A. Tavasoli, T. Wood and G. A. Ozin, *Nat. Commun.*, 2019, **10**(1), 1–12.

3 J. Lin, C. Ma, J. Luo, X. Kong, Y. Xu, G. Ma, J. Wang, C. Zhang, Z. Li and M. Ding, *RSC Adv.*, 2019, **9**, 8684–8694.
4 J. Kopyscinski, T. J. Schildhauer and S. M. A. Biollaz, *Fuel*, 2010, **89**, 1763–1783.
5 W. Gac, W. Zawadzki, M. Kuśmierz, G. Słowik and W. Grudziński, *Appl. Surf. Sci.*, 2023, 157542, DOI: **10.1016/j.apsusc.2023.157542**.
6 W. Gac, W. Zawadzki, G. Słowik, W. Grudziński and S. Dzwigaj, *Catal. Today*, 2024, 114728, DOI: **10.1016/j.cattod.2024.114728**.
7 G. Yergaziyeva, Z. Kuspanov, M. Mambetova, N. Khudaibergenov, N. Makayeva and C. Daulbayev, *J. CO_2 Util.*, 2024, **80**, 102682.
8 M. Younas, L. Loong Kong, M. J. K. Bashir, H. Nadeem, A. Shehzad and S. Sethupathi, *Energy Fuels*, 2016, **30**, 8815–8831.
9 W. Gac, W. Zawadzki, M. Rotko, M. Greluk, G. Słowik and G. Kolb, *Catal. Today*, 2020, **357**, 468–482.
10 M. A. Memon, Y. Jiang, M. A. Hassan, M. Ajmal, H. Wang and Y. Liu, *Catalysts*, 2023, **13**, 1514.
11 K. Jalama, *Catal. Rev.*, 2017, **59**, 95–164.
12 L. P. Merkouri, J. L. Martín-Espejo, L. F. Bobadilla, J. A. Odriozola, M. S. Duyar and T. R. Reina, *Nanomaterials*, 2023, **13**, 506.
13 S. Kumar, K. Singh Grewal and P. Kumar, *A review of current developments in Sabatier reaction-based methanation of carbon dioxide: Thermocatalytic approach*.
14 M. Usman, A. G. Fareed and M. Amin, *J. Iran. Chem. Soc.*, 2024, **21**(5), 1185–1201.
15 Z. Wang, L. Wang, Y. Cui, Y. Xing and W. Su, *J. CO_2 Util.*, 2022, **63**, 102117.
16 L. Shen, J. Xu, M. Zhu and Y. F. Han, *ACS Catal.*, 2020, **10**, 14581–14591.
17 L. Li, W. Zeng, M. Song, X. Wu, G. Li and C. Hu, *Catalysts*, 2022, **12**, 244.
18 G. Busca, E. Spennati, P. Riani and G. Garbarino, *Energies*, 2023, **16**, 5304.
19 N. D. M. Ridzuan, M. S. Shaharun, M. A. Anawar and I. Ud-Din, *Catalysts*, 2022, **12**, 469.
20 M. Usman, S. Podila, M. A. Alamoudi and A. A. Al-Zahrani, *Catalysts*, 2025, **15**, 203.
21 Y. H. Lee, J. Y. Ahn, D. D. Nguyen, S. W. Chang, S. S. Kim and S. M. Lee, *RSC Adv.*, 2021, **11**, 17648–17657.
22 M. A. Memon, W. Zhou, M. Ajmal, A. Afzal, Y. Jiang, C. Zhang, J. Zhang and Y. Liu, *Int. J. Hydrogen Energy*, 2024, **92**, 1202–1213.
23 S. Ewald, M. Kolbeck, T. Kratky, M. Wolf and O. Hinrichsen, *Appl. Catal., A*, 2019, **570**, 376–386.
24 P. Riani, E. Spennati, M. V. Garcia, V. S. Escribano, G. Busca and G. Garbarino, *Int. J. Hydrogen Energy*, 2023, **48**, 24976–24995.
25 M. Mihet, M. Dan, L. Barbu-Tudoran and M. D. Lazar, *Catalysts*, 2021, 443, DOI: **10.3390/catal11040443**.
26 H. Ma, K. Ma, J. Ji, S. Tang, C. Liu, W. Jiang, H. Yue and B. Liang, *Chem. Eng. Sci.*, 2019, 10–21.
27 K. Wang, Y. Men, S. Liu, J. Wang, Y. Li, Y. Tang, Z. Li, W. An, X. Pan and L. Li, *Fuel*, 2021, 121388, DOI: **10.1016/j.fuel.2021.121388**.
28 R. P. Ye, L. Liao, T. R. Reina, J. Liu, D. Chevella, Y. Jin, M. Fan and J. Liu, *Fuel*, 2021, 119151, DOI: **10.1016/j.fuel.2020.119151**.
29 Y. R. Dias and O. W. Perez-Lopez, *Energy Convers. Manage.*, 2020, 112214, DOI: **10.1016/j.enconman.2019.112214**.
30 W. Gac, W. Zawadzki, G. Słowik, A. Sienkiewicz and A. Kierys, *Microporous Mesoporous Mater.*, 2018, **272**, 79–91.
31 H. Liu, Y. Zhou, H. Cui, Z. Cheng and Z. Zhou, *Ind. Eng. Chem. Res.*, 2024, **63**, 10172–10183.
32 G. Garbarino, S. Chitsazan, T. K. Phung, P. Riani and G. Busca, *Appl. Catal., A*, 2015, **505**, 86–97.
33 G. Busca, *Catal. Today*, 2020, **357**, 621–629.
34 H. Zhang, Y. Dong, W. Fang and Y. Lian, *Chin. J. Catal.*, 2013, **34**, 330–335.
35 M. Lee, J. W. Yoon, Y. Kim, J. S. Yoon, H. J. Chae, Y. H. Han and D. W. Hwang, *Appl. Catal., A*, 2018, **562**, 87–93.
36 S. Moussa, M. A. Arribas, P. Concepción and A. Martínez, *Catal. Today*, 2016, **277**, 78–88.
37 J. Uchisawa, A. Obuchi, T. Tango and T. Murakami, *J. Jpn. Pet. Inst.*, 2015, **58**, 9–19.
38 M. A. Alamoudi, H. Almohamadi and K. J. Smith, *Energy Fuels*, 2021, **35**, 10113–10121.
39 W. L. Vrijburg, G. Garbarino, W. Chen, A. Parastaev, A. Longo, E. A. Pidko and E. J. M. Hensen, *J. Catal.*, 2020, **382**, 358–371.
40 H. Zhang, Y. Dong, W. Fang and Y. Lian, *Chin. J. Catal.*, 2013, **34**, 330–335.
41 P. Riani, I. Valsamakis, T. Cavattoni, V. Sanchez Escribano, G. Busca and G. Garbarino, *Appl. Catal., B*, 2021, 119697, DOI: **10.1016/j.apcatb.2020.119697**.
42 S. V. Moghaddam, M. Rezaei, F. Meshkani and R. Daroughegi, *Int. J. Hydrogen Energy*, 2018, **43**, 19038–19046.
43 S. A. D'Ippolito, C. Especel, L. Vivier, F. Epron and C. L. Pieck, *Appl. Catal., A*, 2014, **469**, 532–540.
44 C. Liang, X. Hu, T. Wei, P. Jia, Z. Zhang, D. Dong, S. Zhang, Q. Liu and G. Hu, *Int. J. Hydrogen Energy*, 2019, **44**, 8197–8213.
45 E. Spennati, P. Riani and G. Garbarino, *Catal. Today*, 2023, 114131, DOI: **10.1016/j.cattod.2023.114131**.
46 J. B. Branco, P. E. Brito and A. C. Ferreira, *Chem. Eng. J.*, 2020, **380**, 122465.
47 M. Biset-Peiró, J. Guilera, T. Zhang, J. Arbiol and T. Andreu, *Appl. Catal., A*, 2019, **575**, 223–229.
48 M. A. Salaev, L. F. Liotta and O. V. Vodyankina, *Int. J. Hydrogen Energy*, 2022, **47**, 4489–4535.
49 T. Montini, M. Melchionna, M. Monai and P. Fornasiero, *Chem. Rev.*, 2016, **116**, 5987–6041.
50 M. C. Bacariza, I. Graça, J. M. Lopes and C. Henriques, *ChemCatChem*, 2018, **10**, 2773–2781.
51 W. Gac, W. Zawadzki, M. Greluk, G. Słowik, M. Rotko and M. Kuśmierz, *Catalysts*, 2021, 13, DOI: **10.3390/catal12010013**.
52 X. Wang, L. Zhu, Y. Liu and S. Wang, *Sci. Total Environ.*, 2018, **625**, 686–695.
53 W. Gac, W. Zawadzki, M. Rotko, G. Słowik and M. Greluk, *Top. Catal.*, 2019, **62**, 524–534.

54 Y. Xie, J. Wen, Z. Li, J. Chen, Q. Zhang, P. Ning, Y. Chen and J. Hao, *Green Chem.*, 2023, **25**, 130–152.
55 S. Podila, A. A. Al-Zahrani, N. Pasupulety and M. A. Alamoudi, *Arabian J. Chem.*, 2023, 105235, DOI: **10.1016/j.arabjc.2023.105235**.
56 P. Yan, E. Kennedy and M. Stockenhuber, *Green Chem.*, 2021, **23**, 4673–4684.
57 K. Wang, Y. Men, S. Liu, J. Wang, Y. Li, Y. Tang, Z. Li, W. An, X. Pan and L. Li, *Fuel*, 2021, 121388, DOI: **10.1016/j.fuel.2021.121388**.
58 N. A. Ayub, H. Bahruji and A. H. Mahadi, *RSC Adv.*, 2021, **11**, 31807–31816.
59 A. I. Tsiotsias, N. D. Charisiou, C. Italiano, G. D. Ferrante, L. Pino, A. Vita, V. Sebastian, S. J. Hinder, M. A. Baker, A. Sharan, N. Singh, K. Polychronopoulou and M. A. Goula, *Appl. Surf. Sci.*, 2024, 158945, DOI: **10.1016/j.apsusc.2023.158945**.
60 F. M. Segal, M. F. Correa, R. Bacani, B. Castanheira, M. J. Politi, S. Brochsztain and E. R. Triboni, *Mater. Res.*, 2018, **21**, e20170674.
61 P. Zhu, Q. Chen, Y. Yoneyama and N. Tsubaki, *RSC Adv.*, 2014, **4**, 64617–64624.
62 X. Wang, S. Zhu, S. Wang, J. Wang, W. Fan and Y. Lv, *Appl. Catal., A*, 2018, **568**, 231–241.
63 M. Mihet, M. Dan, L. Barbu-Tudoran and M. D. Lazar, *Catalysts*, 2021, 443, DOI: **10.3390/catal11040443**.
64 X. Yan, T. Hu, P. Liu, S. Li, B. Zhao, Q. Zhang, W. Jiao, S. Chen, P. Wang, J. Lu, L. Fan, X. Deng and Y. X. Pan, *Appl. Catal., B*, 2019, **246**, 221–231.
65 L. Li, L. Jiang, D. Li, J. Yuan, G. Bao and K. Li, *Appl. Catal. O: Open*, 2024, **192**, 206956.
66 G. De Piano, J. J. Andrade Gamboa, A. M. Condó and F. C. Gennari, *Int. J. Hydrogen Energy*, 2024, **56**, 1007–1019.
67 M. Dan, M. Mihet, Z. Tasnadi-Asztalos, A. Imre-Lucaci, G. Katona and M. D. Lazar, *Fuel*, 2015, **147**, 260–268.
68 D. Méndez-Mateos, V. L. Barrio, J. M. Requies and M. Gil-Calvo, *Environ. Sci. Pollut. Res.*, 2024, **31**, 36093–36117.
69 C. Tang, J. Li, X. Yao, J. Sun, Y. Cao, L. Zhang, F. Gao, Y. Deng and L. Dong, *Appl. Catal., A*, 2015, **494**, 77–86.
70 M. Thommes, K. Kaneko, A. V. Neimark, J. P. Olivier, F. Rodriguez-Reinoso, J. Rouquerol and K. S. W. Sing, *Pure Appl. Chem.*, 2015, **87**, 1051–1069.
71 C. Italiano, J. Llorca, L. Pino, M. Ferraro, V. Antonucci and A. Vita, *Appl. Catal., B*, 2020, **264**, 118494.
72 N. L. Visser, J. C. Verschoor, L. C. J. Smulders, F. Mattarozzi, D. J. Morgan, J. D. Meeldijk, J. E. S. van der Hoeven, J. A. Stewart, B. D. Vandegehuchte and P. E. de Jongh, *Catal. Today*, 2023, **418**, 114071.
73 M. Usman, S. Podila and A. A. Al-Zahrani, *Int. J. Hydrogen Energy*, 2024, **95**, 173–184.
74 A. J. Maia, B. Louis, Y. L. Lam and M. M. Pereira, *J. Catal.*, 2010, **269**, 103–109.
75 J. M. Rynkowski, T. Paryjczak and M. Lenik, *Appl. Catal., A*, 1993, **106**, 73–82.
76 T. K. Phung and G. Garbarino, *J. Ind. Eng. Chem.*, 2017, **47**, 288–296.
77 A. Bustinza, M. Frías, Y. Liu and E. García-Bordejé, *Catal. Sci. Technol.*, 2020, **10**, 4061–4071.
78 T. Burger, F. Koschany, A. Wenng, O. Thomys, K. Köhler and O. Hinrichsen, *Catal. Sci. Technol.*, 2018, **8**, 5920–5932.
79 Y. Pan, C. J. Liu and Q. Ge, *Langmuir*, 2008, **24**, 12410–12419.
80 L. Proaño, E. Tello, M. A. Arellano-Trevino, S. Wang, R. J. Farrauto and M. Cobo, *Appl. Surf. Sci.*, 2019, **479**, 25–30.
81 E. García-Bordejé, A. B. Dongil, J. M. Conesa, A. Guerrero-Ruiz and I. Rodríguez-Ramos, *Nanomaterials*, 1052, DOI: **10.3390/nano12071052**.
82 X. Wang, Y. Hong, H. Shi and J. Szanyi, *J. Catal.*, 2016, **343**, 185–195.
83 J. M. Rynkowski, T. Paryjczak and M. Lenik, *Appl. Catal., A*, 1993, **106**, 73–82.
84 C. Yang, J. Zhang, W. Liu, X. Yang, Y. Wang and W. Wang, *J. Catal.*, 2024, 115811, DOI: **10.1016/j.jcat.2024.115811**.
85 S. López-Rodríguez, A. Davó-Quiñonero, E. Bailón-García, D. Lozano-Castelló, I. J. Villar-Garcia, V. P. Dieste, J. A. O. Calvo, J. R. G. Velasco and A. Bueno-López, *J. CO_2 Util.*, 2022, **60**, 101980.
86 D. Méndez-mateos, V. Laura Barrio, J. M. Requies and J. F. Cambra, *Catalysts*, 2021, **11**, 1–28.
87 A. I. Tsiotsias, N. D. Charisiou, A. AlKhoori, S. Gaber, V. Stolojan, V. Sebastian, B. van der Linden, A. Bansode, S. J. Hinder, M. A. Baker, K. Polychronopoulou and M. A. Goula, *J. Energy Chem.*, 2022, **71**, 547–561.
88 A. Cárdenas-Arenas, A. Quindimil, A. Davó-Quiñonero, E. Bailón-García, D. Lozano-Castelló, U. De-La-Torre, B. Pereda-Ayo, J. A. González-Marcos, J. R. González-Velasco and A. Bueno-López, *Appl. Mater. Today*, 2020, **19**, 100591.
89 M. C. Biesinger, B. P. Payne, A. P. Grosvenor, L. W. M. Lau, A. R. Gerson and R. S. C. Smart, *Appl. Surf. Sci.*, 2011, **257**, 2717–2730.
90 Y. He, H. Shen, Y. Bai, X. Niu, Y. Zhao, C. Wu, S. Yang, Y. Cao, Q. Zhang and H. Zhang, *Ind. Eng. Chem. Res.*, 2022, **61**, 15948–15960.
91 W. Gac, W. Zawadzki, M. Rotko, G. Słowik and M. Greluk, *Top. Catal.*, 2019, **62**, 524–534.
92 X. Guo, A. Traitangwong, M. Hu, C. Zuo, V. Meeyoo, Z. Peng and C. Li, *Energy Fuels*, 2018, **32**, 3681–3689.
93 S. V. Moghaddam, M. Rezaei, F. Meshkani and R. Daroughegi, *Int. J. Hydrogen Energy*, 2018, **43**, 19038–19046.
94 Y. Xu, Y. Wu, J. Li, S. Wei, X. Gao and P. Wang, *Int. J. Hydrogen Energy*, 2021, **46**, 20919–20929.
95 J. Lin, C. Ma, Q. Wang, Y. Xu, G. Ma, J. Wang, H. Wang, C. Dong, C. Zhang and M. Ding, *Appl. Catal., B*, 2019, **243**, 262–272.
96 R. Y. Chein and C. C. Wang, *Catalysts*, 2020, **10**, 1112.
97 L. Zhou, Q. Wang, L. Ma, J. Chen, J. Ma and Z. Zi, *Catal. Lett.*, 2015, **145**, 612–619.
98 A. Rajabzadeh Nobakht, M. Rezaei, S. M. Alavi, E. Akbari, M. Varbar and J. Hafezi-Bakhtiari, *Int. J. Hydrogen Energy*, 2023, **48**, 38664–38675.